Adaptive lattice Boltzmann model for compressible flows: Viscous and conductive properties

Chenghai Sun
State Key Laboratory of Tribology, Department of Engineering Mechanics, Tsinghua University, Beijing 100084, People's Republic of China

(Received 9 July 1999; revised manuscript received 24 September 1999)

This paper presents an adaptive lattice Boltzmann model of higher accuracy for viscous compressible flows with heat conduction. The proper heat conduction term in the energy equation is recovered by a modification of the kinetic energy transported by particles. The accuracy of the model is improved by introducing a term of fluctuating velocity in the collision-invariant vector. The Navier-Stokes equations are derived by the Chapman-Enskog method from the Bhatnagar-Gross-Krook Boltzmann equation. The advantage of an adaptive lattice Boltzmann model over the standard ones is that the particle velocities are no longer constant, varying with the mean velocity and internal energy. Therefore, the mean flow can have a high Mach number. To investigate the viscous and conductive properties of the model, a one-dimensional flow with a sinusoidal velocity distribution and Couette flow were simulated, showing good agreement with the analytical solutions. The simulation of an oblique shock impinging on a solid wall has captured the complex feature of the interaction between the shock and boundary layer.

PACS number(s): 47.40.Nm, 51.20.+d, 47.15.Cb

I. INTRODUCTION

The lattice Boltzmann (LB) method as a relatively new numerical scheme has recently achieved considerable success in simulating fluid flows and associated transport phenomena. A variety of LB models for different physical problems, such as single component hydrodynamics, multiphase and multicomponent fluids, magnetohydrodynamics, reaction-diffusion systems, flows through porous media, and other complex systems have been established [1]. The LB method has demonstrated a significant potential and broad applicability with numerous computational advantages, such as the parallel algorithm and simplicity of programming. There was one recent attempt to overcome the low Mach number constraint, so that the LB method may simulate supersonic flows with a shock wave [2,3].

Historically, the LB method originated from a Boolean model known as lattice gas automata (LGA) [4,5]. The standard LGA models impose, for the sake of computational efficiency, a Boolean constraint which restricts the number of particles with a given velocity at a site to be zero or 1. The local equilibrium of the mean population of particles is described by the Fermi-Dirac statistics. As a result, LGA models suffer from statistical noise and non-Galilean invariance. These difficulties have led to the development of LB models [6–8]. In the LB method real numbers represent the local ensemble-averaged particle distribution functions. A simple Bhatnagar-Gross-Krook (BGK) collision operator is applied [6,7]. Space and time are discrete as in the LGA method. The particle velocities belong to a finite set. Consequently the macroscopic velocity is limited, and, in turn, the general LB method suffers from the constraint of small Mach number. In the past years, the gas-kinetic theory [9,10] and the discrete-velocity model [11] successfully simulated the compressible Euler equation. The finite volume method was employed to solve the Boltzmann equations. The discontinuities were well captured. However, due to the restraint mentioned above, the standard LB method has a great difficulty in simulating compressible Euler flows at high Mach number. Efforts have been made to solve this problem. Alexander *et al.* [12] attempted to decrease the sound speed to augment the Mach number. Qian and Orszag [13] studied the nonlinear deviation of the LB model in a compressible regime, and presented a numerical simulation of a shock profile. Yan and co-workers [3,14] proposed a compressible LB model for the Euler system, and successfully simulated the Sod shock-tube problem in which a membrane separates a long tube with high-pressure and high-density fluid in one side and low-pressure and low-density fluid in the other side, and the membrane blasts at initial time [24]. Recently, we proposed a locally adaptive semidiscrete LB model [2]. The particle velocity set is chosen according to the fluid local velocity and internal energy. The fluid velocity is no longer limited by the particle velocity set. Consequently, the model is suitable for a wide range of Mach numbers. Simulations of the Sod shock-tube problem and two-dimensional shock reflection demonstrated the model's capability for solving compressible Euler flows with shocks. The Navier-Stokes equations were derived by the Chapman-Enskog method. However, the heat conduction term in the energy equation was not clearly formulated.

The objectives of the present paper are to establish a modified semidiscrete adaptive LB model to recover the correct heat conduction term in the energy equation, to study the viscous term in the Navier-Stokes equations, and to improve the accuracy. This paper is organized as follows. Section II describes a LB model with adaptive particle velocities first, then derives general macroscopic conservation equations from the Boltzmann equations by the Chapman-Enskog method, defines the equilibrium distribution function to obtain the Navier-Stokes equations, and finally eliminates the discretion errors. Section III is about the numerical results. Finally, some concluding remarks will be presented.

II. SEMIDISCRETE ADAPTIVE LB MODEL

A. Basic equations

Let $\mathbf{r}$ be the particle ''migrating velocity,'' transporting a particle from a node to its neighbor node at a distance $\mathbf{r}\Delta t$

during the discrete time Δt. The migrating velocity set $\{\mathbf{r}\}$ is discrete because the nodes of the lattice are discrete. Suppose that the particle transports the mass m, momentum $\boldsymbol{\xi}$, and energy ζ to the neighbor node at a distance $\mathbf{r}\Delta t$, where $\boldsymbol{\xi} \in \mathcal{D}_1$, $\mathcal{D}_1$ is a bounded domain in $\mathbb{R}^3$ (or in $\mathbb{R}^2$ for two-dimensional models) and $\mathbf{r} \in \mathcal{D}_1$; $m \in \mathcal{D}_0$, $\zeta \in \mathcal{D}_0$, $\mathcal{D}_0$ is a bounded domain in $\mathbb{R}$. Define $\mathcal{D}=\mathcal{D}_0 \times \mathcal{D}_1 \times \mathcal{D}_0$. Obviously, m, $\boldsymbol{\xi}$, and ζ can vary continuously. In the standard LB model, space, time, and the particle velocity are all discrete; therefore, m, $\boldsymbol{\xi}$, and ζ must be discrete and take the values 1, $\mathbf{r}$, and $\frac{1}{2}\mathbf{r}^2$, respectively. The objective of introducing such a semidiscrete velocity LB model is to increase the accuracy of the model.

Let $\mathbf{x}$ be an arbitrary node of a lattice; $\mathbf{x}$tf($\mathbf{x}$,$\mathbf{r}$,m,$\boldsymbol{\xi}$,ζ,t) is the density distribution function for the particle with the migrating velocity $\mathbf{r}$, moving to $\mathbf{x}$tx+$\mathbf{r}\Delta$t during Δt, and transporting the mass m, momentum $\boldsymbol{\xi}$, and energy ζ. The conserved total mass, momentum, and energy are defined as

$$\rho \equiv \sum_{\mathbf{r}} \int_{\mathcal{D}} m f(\mathbf{x},\mathbf{r},m,\boldsymbol{\xi},\zeta,t)\, dm\, d\boldsymbol{\xi}\, d\zeta, \tag{1}$$

$$\rho \mathbf{v} \equiv \sum_{\mathbf{r}} \int_{\mathcal{D}} \boldsymbol{\xi} f(\mathbf{x},\mathbf{r},m,\boldsymbol{\xi},\zeta,t)\, dm\, d\boldsymbol{\xi}\, d\zeta, \tag{2}$$

$$\rho E \equiv \sum_{\mathbf{r}} \int_{\mathcal{D}} \zeta f(\mathbf{x},\mathbf{r},m,\boldsymbol{\xi},\zeta,t)\, dm\, d\boldsymbol{\xi}\, d\zeta, \tag{3}$$

where $d\boldsymbol{\xi}=d\xi_1 d\xi_2 d\xi_3$. Define

$$\boldsymbol{\eta} \equiv [m,\boldsymbol{\xi},\zeta], \tag{4}$$

$$f(\mathbf{x},\mathbf{r},\boldsymbol{\eta},t) \equiv f(\mathbf{x},\mathbf{r},m,\boldsymbol{\xi},\zeta,t), \tag{5}$$

$$\mathbf{Y} \equiv [\rho,\rho\mathbf{v},\rho E]. \tag{6}$$

Equations (1), (2), and (3) can be written in a compact form

$$\mathbf{Y} = \sum_{\mathbf{r}} \int_{\mathcal{D}} \boldsymbol{\eta} f(\mathbf{x},\mathbf{r},\boldsymbol{\eta},t)\, d\boldsymbol{\eta}, \tag{7}$$

where $d\boldsymbol{\eta}=dm\,d\boldsymbol{\xi}\,d\zeta$.

In LB models, the Boltzmann equation is written as

$$f(\mathbf{x}+\mathbf{r}\Delta t,\mathbf{r},\boldsymbol{\eta},t+\Delta t) - f(\mathbf{x},\mathbf{r},\boldsymbol{\eta},t) = \Omega, \tag{8}$$

where

$$\Omega = -\frac{1}{\tau}[f(\mathbf{x},\mathbf{r},\boldsymbol{\eta},t) - f^{\mathrm{eq}}(\mathbf{x},\mathbf{r},\boldsymbol{\eta},t)], \tag{9}$$

and $f^{\mathrm{eq}}(\mathbf{x},\mathbf{r},\boldsymbol{\eta},t)$ is the equilibrium distribution depending on the total mass, momentum, and energy. Because the discrete migrating velocity set $\{\mathbf{r}\}$ is large, and $\boldsymbol{\eta}$ can vary continuously, the Boltzmann equation (8), in general, is hard to solve. In fact, Eq. (8) is only used for theoretical analysis. The technique for numerical simulation will be discussed in Sec. III.

In the following, we utilize the Chapman-Enskog expansion of the solution of Eq. (8) [2,15,16] to derive the macroscopic conservation equations. We choose $\Delta t = \epsilon T$, where T is a reference time scale and ϵ a typical small parameter. We are then looking for a solution of Eq. (8) as an asymptotic expansion of the forms

$$f = \sum_{n=0}^{\infty} \epsilon^n f^{(n)}, \tag{10}$$

$$\frac{\partial \mathbf{Y}}{\partial t} = \sum_{n=0}^{\infty} \epsilon^n \mathbf{F}^{(n)}, \tag{11}$$

where $f^{(n)}$ and $\mathbf{F}^{(n)}$ depend only on $\mathbf{Y}$ and its successive gradients. $f^{(0)}=f^{\mathrm{eq}}$ is completely determined by the macroscopic variables ρ, $\rho\mathbf{v}$, and ρE, and verifies

$$\mathbf{Y} = \sum_{\mathbf{r}} \int_{\mathcal{D}} \boldsymbol{\eta} f^{\mathrm{eq}}(\mathbf{x},\mathbf{r},\boldsymbol{\eta},t)\, d\boldsymbol{\eta}. \tag{12}$$

Considering relations (7), (12), (10), and (9) we have

$$\sum_{\mathbf{r}} \int_{\mathcal{D}} \boldsymbol{\eta} f^{(n)}\, d\boldsymbol{\eta} = 0, \quad \forall n \geqslant 1, \tag{13}$$

$$\sum_{\mathbf{r}} \int_{\mathcal{D}} \boldsymbol{\eta} \Omega\, d\boldsymbol{\eta} = 0. \tag{14}$$

A vector $\boldsymbol{\eta}$ verifying Eq. (14) is called the collision invariant.

We Taylor expand the left-hand side of Eq. (8). Then, by identifying the first order terms of ϵ, we can determine $f^{(1)}$, and, considering Eqs. (13) and (14), we obtain $\mathbf{F}^{(0)}$ and $\mathbf{F}^{(1)}$:

$$f^{(1)} = -\tau T\left(\boldsymbol{\nabla} f^{\mathrm{eq}} \cdot \mathbf{r} + \frac{\partial f^{\mathrm{eq}}}{\partial \mathbf{Y}} \cdot \mathbf{F}^{(0)}\right),$$

$$\mathbf{F}^{(0)} = -\operatorname{div} \sum_{\mathbf{r}} \int_{\mathcal{D}} \mathbf{r} f^{\mathrm{eq}} \boldsymbol{\eta}\, d\boldsymbol{\eta},$$

$$\mathbf{F}^{(1)} = -\operatorname{div} \sum_{\mathbf{r}} \int_{\mathcal{D}} \left\{ f^{(1)}\mathbf{r} + \frac{T}{2}\left[\operatorname{div}(f^{\mathrm{eq}}\mathbf{r}\mathbf{r}) + \frac{\partial f^{\mathrm{eq}}}{\partial \mathbf{Y}} \cdot \mathbf{F}^{(0)}\mathbf{r}\right]\right\} \times \boldsymbol{\eta}\, d\boldsymbol{\eta}.$$

The operators div and $\boldsymbol{\nabla}$ take effect on variable $\mathbf{x}$. The variables $\mathbf{r}$, $\boldsymbol{\xi}$, and ζ are independent of $\mathbf{x}$. Therefore, they can be treated as constant for div and $\boldsymbol{\nabla}$. Up to order 1 Eq. (11) is written as

$$\frac{\partial \mathbf{Y}}{\partial t} = -\operatorname{div} \sum_{\mathbf{r}} \int_{\mathcal{D}} f^{\mathrm{eq}} \mathbf{r}\boldsymbol{\eta}\, d\boldsymbol{\eta} - \epsilon T\left(\frac{1}{2} - \tau\right) \operatorname{div} \times \left[\operatorname{div} \sum_{\mathbf{r}} \int_{\mathcal{D}} f^{\mathrm{eq}} \mathbf{r}\mathbf{r}\boldsymbol{\eta}\, d\boldsymbol{\eta} + \sum_{\mathbf{r}} \int_{\mathcal{D}} \frac{\partial f^{\mathrm{eq}}}{\partial \mathbf{Y}} \cdot \mathbf{F}^{(0)} \mathbf{r}\boldsymbol{\eta}\, d\boldsymbol{\eta}\right] + O(\epsilon^2). \tag{15}$$

This is the macroscopic conservation equation. It depends on the distribution of f^{eq}. If the equilibrium distribution is properly determined, it may become the Navier-Stokes equation.

B. Equilibrium distributions

On a uniform lattice, let us consider the symmetric vector set $\{\mathbf{c}'_{j\nu}; j=1,\ldots,b_\nu\}$ connecting a node to its equal distance neighbor nodes, where b_ν is the number of vector di-

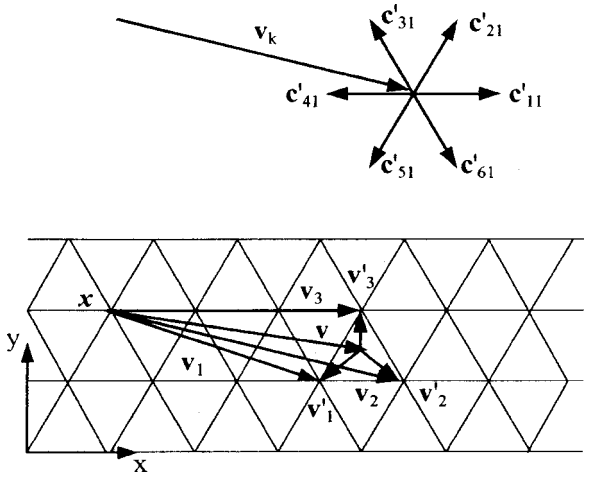

FIG. 1. Particle velocities.

rections. For a hexagonal lattice we choose $b_\nu=6$, and $\nu=1$ and 2. The module of $\mathbf{c}'_{j\nu}$ is c'_ν. In the standard LB method, the constant vectors $\mathbf{c}'_{j\nu}$ are the particle velocities. The basic idea of what we call an ''adaptive LB model'' is to superimpose the fluid velocity $\mathbf{v}$, which is approximated by $\mathbf{v}_k$ $(k=1,2,3)$ (see Fig. 1), on the symmetric velocity $\mathbf{c}'_{j\nu}$. Let $\mathbf{x}$ be an arbitrary node; $\mathbf{v}$ is the fluid velocity at this node; and $\mathbf{v}_1$, $\mathbf{v}_2$, and $\mathbf{v}_3$ are the vectors from the node $\mathbf{x}$ to the apexes of the triangle containing the velocity vector $\mathbf{v}$. We introduce the particle velocities $\mathbf{c}_{j\nu k}, \overline{\mathbf{c}}_{j\nu}$ and the fluctuating velocities $\mathbf{v}'_k$ $(k=1,2,3)$:

$$\mathbf{c}_{j\nu k}=\mathbf{v}_k+\mathbf{c}'_{j\nu}, \tag{16}$$

$$\overline{\mathbf{c}}_{j\nu}=\mathbf{v}+\mathbf{c}'_{j\nu}, \tag{17}$$

$$\mathbf{v}_k=\mathbf{v}+\mathbf{v}'_k. \tag{18}$$

In standard LB models, the particle velocities are constant, therefore, the mean velocity (i.e., the fluid velocity) is limited. In the present model, the particle velocities are adapted to the mean velocity, which is then rid of the constraint of the particle velocities. For high speed flow the fluctuating velocities $\mathbf{v}'_k$ is small.

In the following, we will determine the equilibrium distribution f^{eq}. We hope the model is as simple as possible under the condition that the correct macroscopic equations (Navier-Stokes equations) can be obtained. We concentrate the particles at $\mathbf{r}=\mathbf{c}_{j\nu k}$, $m=m_{j\nu k}$, $\boldsymbol{\xi}=\boldsymbol{\xi}_{j\nu k}$ and $\zeta=\zeta_{j\nu k}$. $m_{j\nu k}$, $\boldsymbol{\xi}_{j\nu k}$, and $\zeta_{j\nu k}$ are determined by the macroscopic variables ρ, $\mathbf{v}$, and E. For $\mathbf{r}=\mathbf{c}_{j\nu k}$, we define

$$f^{\mathrm{eq}}_{j\nu k}(\mathbf{x},\boldsymbol{\eta},t)\equiv f^{\mathrm{eq}}(\mathbf{x},\mathbf{c}_{j\nu k},\boldsymbol{\eta},t), \tag{19}$$

and for other $\mathbf{r}$'s we set $f^{\mathrm{eq}}(\mathbf{x},\mathbf{r},\boldsymbol{\eta},t)=0$. We suppose $f^{\mathrm{eq}}_{j\nu k}(\mathbf{x},\boldsymbol{\eta},t)$ to have the form

$$f^{\mathrm{eq}}_{j\nu k}(\mathbf{x},\boldsymbol{\eta},t)=d_{\nu k}\delta(m-m_{j\nu k})\,\delta(\boldsymbol{\xi}-\boldsymbol{\xi}_{j\nu k})\,\delta(\zeta-\zeta_{j\nu k}), \tag{20}$$

where $\delta(\boldsymbol{\xi})$ is the δ function. $\delta(\boldsymbol{\xi})=0$ for $\boldsymbol{\xi}\neq\mathbf{0}$; $\int g(\boldsymbol{\xi})\delta(\boldsymbol{\xi})d\boldsymbol{\xi}=g(\mathbf{0})$. $\delta(\zeta)=0$ for $\zeta\neq 0$; $\int g(\zeta)\delta(\zeta)d\zeta=g(0)$. Equation (15) becomes

$$\frac{\partial\mathbf{Y}}{\partial t}=-\operatorname{div}\sum_{k,\nu,j}\left\{d_{\nu k}\mathbf{c}_{j\nu k}\boldsymbol{\eta}_{j\nu k}+\epsilon T\left(\frac{1}{2}-\tau\right)\times\left[\operatorname{div}(d_{\nu k}\mathbf{c}_{j\nu k}\mathbf{c}_{j\nu k}\boldsymbol{\eta}_{j\nu k})+\mathbf{F}^{(0)}\cdot\frac{\partial}{\partial\mathbf{Y}}(d_{\nu k}\mathbf{c}_{j\nu k}\boldsymbol{\eta}_{j\nu k})\right]\right\}+O(\epsilon^2), \tag{21}$$

where $O(\epsilon^2)$ is the error term derived in the Chapman-Enskog expansion, and

$$\boldsymbol{\eta}_{j\nu k}=[m_{j\nu k},\boldsymbol{\xi}_{j\nu k},\zeta_{j\nu k}]. \tag{22}$$

After substituting $f^{\mathrm{eq}}_{j\nu k}$ into it, Eq. (12) becomes

$$\mathbf{Y}=\sum_{k,\nu,j} d_{\nu k}\boldsymbol{\eta}_{j\nu k}. \tag{23}$$

In Ref. [2], in order to obtain an arbitrary special heat ratio γ, we introduced the particle potential energy Φ and assumed that the total energy of a particle consists of kinetic energy and potential energy, i.e., $\zeta_{j\nu k}=\frac{1}{2}\overline{\mathbf{c}}^2_{j\nu}+\Phi=\frac{1}{2}(v^2+2\mathbf{c}'_{j\nu}\cdot\mathbf{v}+c'^2_\nu)+\Phi$. However, because of the fluctuating kinetic energy $\frac{1}{2}c'^2_\nu$, the heat conduction term in the energy equation could not be properly formulated. To overcome this difficulty, now we replace c'^2_ν by a mean value $\overline{c'^2}$, i.e.,

$$\zeta_{j\nu k}=\frac{1}{2}(v^2+2\mathbf{c}'_{j\nu}\cdot\mathbf{v}+\overline{c'^2})+\Phi, \tag{24}$$

where

$$\overline{c'^2}=\frac{1}{\rho}\sum_{k,\nu} mb_\nu d_{\nu k}c'^2_\nu. \tag{25}$$

In Ref. [2], $\boldsymbol{\xi}_{j\nu k}$ was chosen as $\boldsymbol{\xi}_{j\nu k}=\overline{\mathbf{c}}_{j\nu}$. However, the Navier-Stokes equation had discretion error terms $\mathbf{v}'_k\mathbf{v}'_k$. These terms can be eliminated if a correction term is added to $m_{j\nu k}$, $\boldsymbol{\xi}_{j\nu k}$, and $\zeta_{j\nu k}$. For comparison we describe two models: model I without correction and model II with correction. Model I:

$$m^{\mathrm{I}}_{j\nu k}=1, \tag{26}$$

$$\boldsymbol{\xi}^{\mathrm{I}}_{j\nu k}=\overline{\mathbf{c}}_{j\nu}, \tag{27}$$

$$\zeta^{\mathrm{I}}_{j\nu k}=\frac{1}{2}(v^2+2\mathbf{c}'_{j\nu}\cdot\mathbf{v}+\overline{c'^2})+\Phi, \tag{28}$$

$$\boldsymbol{\eta}^{\mathrm{I}}_{j\nu k}=[m^{\mathrm{I}}_{j\nu k},\boldsymbol{\xi}^{\mathrm{I}}_{j\nu k},\zeta^{\mathrm{I}}_{j\nu k}]. \tag{29}$$

Model II:

$$m^{\mathrm{II}}_{j\nu k}=m^{\mathrm{I}}_{j\nu k}-\chi_{j\nu k}, \tag{30}$$

$$\boldsymbol{\xi}^{\mathrm{II}}_{j\nu k}=\boldsymbol{\xi}^{\mathrm{I}}_{j\nu k}-\chi_{j\nu k}\mathbf{v}, \tag{31}$$

$$\zeta^{\mathrm{II}}_{j\nu k}=\zeta^{\mathrm{I}}_{j\nu k}-\chi_{j\nu k}\left[\frac{1}{2}(v^2+\overline{c'^2})+\Phi\right], \tag{32}$$

$$\boldsymbol{\eta}^{\mathrm{II}}_{j\nu k}=[m^{\mathrm{II}}_{j\nu k},\boldsymbol{\xi}^{\mathrm{II}}_{j\nu k},\zeta^{\mathrm{II}}_{j\nu k}], \tag{33}$$

where D is the space dimension and

$$\chi_{j\nu k}=\frac{D}{2c_\nu'^2}(\mathbf{c}_{j\nu}'\cdot\mathbf{v}_k'). \tag{34}$$

In order to increase the accuracy it is assumed that ρ_k satisfy the equations

$$\rho=\sum_{k=1}^{3}\rho_k, \tag{35}$$

$$\rho\mathbf{v}=\sum_{k=1}^{3}\rho_k\mathbf{v}_k, \tag{36}$$

where $\rho_k=\Sigma_\nu b_\nu d_{\nu k}$. For a given ρ and $\rho\mathbf{v}$ it can be proved that Eqs. (35) and (36) have unique non-negative solutions for ρ_k (see Fig. 1). Equations (35) and (36) permit us to write.

$$\sum_k \rho_k\mathbf{v}_k'=\mathbf{0}. \tag{37}$$

Thanks to Eq. (37), the first order of $\mathbf{v}_k'$ in the conservation equations disappears.

Substituting $\boldsymbol{\eta}_{j\nu k}^{\mathrm{I}}$ and $\boldsymbol{\eta}_{j\nu k}^{\mathrm{II}}$ into Eq. (23) that has to be satisfied, one has the same equations for these two models:

$$\rho=\sum_{k,\nu} b_\nu d_{\nu k}=\sum_{k=1}^{3}\rho_k, \tag{38}$$

$$\rho E=\frac{1}{2}\rho v^2+\sum_{k,\nu}\frac{1}{2}b_\nu d_{\nu k}c_\nu'^2+\rho\Phi, \tag{39}$$

The second component of Eq. (23) is automatically satisfied as long as $d_{\nu k}$ satisfies Eq. (38) which is identical to Eq. (35). This expression for ρE is the same as that of Ref. [2], although the vector $\boldsymbol{\eta}_{j\nu k}$ is different. We introduce the density portion $\alpha_k\equiv\rho_k/\rho$, and suppose $d_{\nu k}$ to have the form

$$d_{\nu k}=\alpha_k d_\nu, \tag{40}$$

where $d_\nu=\Sigma_k d_{\nu k}$ will be determined by the density and the pressure (or internal energy).

A perfect gas with a specific heat ratio γ satisfies $p=(\gamma-1)\rho e$, where $e=E-\frac{1}{2}v^2$ is the internal energy. The pressure p has the form

$$p=\sum_\nu b_\nu d_\nu\frac{1}{D}c_\nu'^2. \tag{41}$$

In the case where c_ν' have two levels ($\nu=1$ and 2) one can determine d_1, d_2, and Φ by Eqs. (35), (39) and (41):

$$d_1=\rho\frac{c_2'^2-D(\gamma-1)e}{b_1(c_2'^2-c_1'^2)},$$

$$d_2=\rho\frac{D(\gamma-1)e-c_1'^2}{b_2(c_2'^2-c_1'^2)},$$

$$\Phi=\left[1-\frac{D}{2}(\gamma-1)\right]e.$$

In order to ensure the positivity of d_1 and d_2, c_1' and c_2' are required to satisfy $c_1'^2<D(\gamma-1)e<c_2'^2$. However, c_1' and c_2' are not completely determined. In practice, c_1' is set to be the integer part of $\sqrt{D(\gamma-1)e}$, and $c_2'=c_1'+1$. For a two-dimensional Boltzmann model without particle potential energy the special heat ratio γ is 2 [11]. From the relation above it can be seen that $\Phi=0$ when $\gamma=2$, agreeing with the standard LB models. When e is small, c_1' may be zero. The correction terms in Eqs. (30), (31), and (32) have to be modified if $c_1'=0$. In this case, $\chi_{j\nu k}$ in Eq. (34) is defined as

$$\chi_{j1k}=0,\quad \chi_{j2k}=\frac{d_1+d_2}{d_2}\frac{D}{2c_2'^2}(\mathbf{c}_{j2}'\cdot\mathbf{v}_k'),\quad \text{if } c_1'=0. \tag{42}$$

Now, the equilibrium is completely determined. Considering relations (16), (17), (18), (36), and (37), the continuity, momentum and energy equations are derived for models I and II after substituting $\boldsymbol{\eta}_{j\nu k}^{\mathrm{I}}$ and $\boldsymbol{\eta}_{j\nu k}^{\mathrm{II}}$ into Eq. (21):

$$\frac{\partial\rho}{\partial t}+\mathrm{div}(\rho\mathbf{v})=\mathrm{div}(\mathbf{B}_0)+O(\epsilon^2), \tag{43}$$

$$\frac{\partial\rho\mathbf{v}}{\partial t}+\mathrm{div}(\rho\mathbf{v}\mathbf{v})+\nabla p=\mathrm{div}\{\mu[\nabla\mathbf{v}+(\nabla\mathbf{v})^T-(\gamma-1)\mathrm{div}\,\mathbf{v}\mathbf{I}_d]+\mathbf{B}_1\}+O(\epsilon^2), \tag{44}$$

$$\frac{\partial\rho E}{\partial t}+\mathrm{div}(p\mathbf{v}+\rho E\mathbf{v})=\mathrm{div}\{\mu\mathbf{v}\cdot[\nabla\mathbf{v}+(\nabla\mathbf{v})^{\mathrm{T}}-(\gamma-1)\mathrm{div}\,\mathbf{v}\mathbf{I}_d]\}+\mathrm{div}\{\kappa\nabla e-(\gamma-1)e\nabla\kappa+\mathbf{B}_2\}+O(\epsilon^2), \tag{45}$$

where

$$\mu=\kappa=\epsilon T\left(\tau-\frac{1}{2}\right)\sum_\nu b_\nu d_\nu\frac{1}{D}c_\nu'^2. \tag{46}$$

μ and κ are the viscosity and heat conductivity, respectively; ϵT is the time step; and $O(\epsilon^2)$, the error terms derived in the Chapman-Enskog expansion, are of higher order than the viscous term and heat conduction term in Eqs. (44) and (45) (see Eq. (46)). For model I,

$$\mathbf{B}_0=\epsilon T\left(\tau-\frac{1}{2}\right)\mathrm{div}\sum_{k,\nu} b_\nu d_{\nu k}\mathbf{v}_k'\mathbf{v}_k',$$

$$\mathbf{B}_1=\epsilon T\left(\tau-\frac{1}{2}\right)\mathrm{div}\sum_{k,\nu} b_\nu d_{\nu k}\mathbf{v}\mathbf{v}_k'\mathbf{v}_k',$$

$$\mathbf{B}_2=\epsilon T\left(\tau-\frac{1}{2}\right)\mathrm{div}\sum_{k,\nu} b_\nu d_{\nu k}\left[\frac{1}{2}(v^2+\overline{c'^2})+\Phi\right]\mathbf{v}_k'\mathbf{v}_k';$$

TABLE I. Comparison between measured viscosities (ν_{I} for model I and ν_{II} for model II) and analytical viscosity (ν_{a}) for different e on 200×4 lattice. Numbers in brackets represent powers of 10.

e	0.5	1.0	1.5	2.0	2.5	3.0
ν_{a}	9.9691[−5]	1.9938[−4]	2.9907[−4]	3.9876[−4]	4.9845[−4]	5.9815[−4]
ν_{I}	1.1480[−4]	2.1406[−4]	3.2634[−4]	4.1933[−4]	5.1528[−4]	6.1124[−4]
ν_{II}	1.0063[−4]	1.9997[−4]	3.0715[−4]	3.9802[−4]	4.9695[−4]	5.9610[−4]
error I	15.15%	7.36%	9.12%	5.16%	3.38%	2.19%
error II	0.942%	0.296%	2.70%	0.186%	0.301%	0.343%

and for model II we have

$$\mathbf{B}_0=\mathbf{B}_1=\mathbf{B}_2=\mathbf{0}$$

due to the relation

$$\sum_{k,\nu,j} d_{\nu k}\mathbf{c}_{j\nu k}\mathbf{c}_{j\nu k}\frac{D}{2c'^2_\nu}(\mathbf{c}'_{j\nu}\cdot\mathbf{v}'_k)$$

$$=\sum_{k,\nu,j} d_{\nu k}\frac{D}{2c'^2_\nu}(\mathbf{c}'_{j\nu}\mathbf{c}'_{j\nu}+\mathbf{c}'_{j\nu}\mathbf{v}_k+\mathbf{v}_k\mathbf{c}'_{j\nu}+\mathbf{v}_k\mathbf{v}_k)(\mathbf{c}'_{j\nu}\cdot\mathbf{v}'_k)$$

$$=\sum_{k,\nu} b_\nu d_{\nu k}\mathbf{v}'_k\mathbf{v}'_k. \tag{47}$$

In Eq. (45) the first term and the second term on the right-hand side correspond, respectively to the dissipation and the heat conduction. Since we replaced the fluctuating kinetic energy c'^2_ν in the collision-invariant vector by the mean value $\overline{c'^2}$, we obtain the correct heat conduction term $\mathrm{div}(\kappa\nabla e)$, which was in the form $\Delta\Sigma_\nu b_\nu d_\nu[1/(2D)]c'^4_\nu$ in Ref. [2], where Δ is the Laplace operator. For model I, $\mathbf{B}_0$, $\mathbf{B}_1$, and $\mathbf{B}_2$ can be regarded as discretion errors; and for model II these errors are eliminated. Then Eqs. (43), (44), and (45) become Navier-Stokes equations.

III. NUMERICAL SIMULATIONS

When $\tau=1$ the Boltzmann equation (8) becomes

$$f(\mathbf{x}+\mathbf{r}\Delta t,\mathbf{r},\boldsymbol{\eta},t+\Delta t)=f^{\mathrm{eq}}(\mathbf{x},\mathbf{r},\boldsymbol{\eta},t). \tag{48}$$

Since f^{eq} depends only on fluid density, velocity, and internal energy, the particle distribution f at $t+\Delta t$ is also determined by them, independent of the particle distribution f at time t. In this way, the need for computer memory and computation time is considerably reduced. In fact, during the numerical simulations, what we care about are the mass, momentum, and energy transported by the particles, and there is no need to store the particle distribution f. Due to the fact that $f^{\mathrm{eq}}=0$ for $\mathbf{r}\neq\mathbf{c}_{j\nu k}$, the mass, momentum, and energy transported by the particles from a node to $\mathbf{x}+\mathbf{c}_{j\nu k}\Delta t$ are components of the vector

$$\int_{\mathcal{D}}\boldsymbol{\eta}f^{\mathrm{eq}}(\mathbf{x},\mathbf{c}_{j\nu k},\boldsymbol{\eta},t)d\boldsymbol{\eta}=\boldsymbol{\eta}_{j\nu k}d_{\nu k}. \tag{49}$$

The following simulations are carried out under the condition $\tau=1$ and $\gamma=1.4$.

A. Viscosity comparison of the two models

Let us consider a special analytical solution of Eq. (44). Suppose $\nabla p=0$, $u=0$, and v to be a function of x. When the variation of the viscosity μ is neglected, Eq. (44) becomes

$$\frac{\partial v}{\partial t}=\nu\frac{\partial^2 v}{\partial x^2}, \tag{50}$$

where $\nu=\mu/\rho$. Equation (50) admits the following analytical solution for the sinusoidal initial condition:

$$v(x,t)=b\exp(-\nu t)\sin(2\pi x/L). \tag{51}$$

The simulation was carried out on a hexagonal lattice of 200×4 nodes, and b is set to be 0.3. From solution (51), we have

$$\ln[v(x,t)/v(x,0)]=-\nu t. \tag{52}$$

When the simulation value of $\ln[v(x,t)/v(x,0)]$ is plotted versus t, a straight line is anticipated, and the slope is $-\nu$. In this way, the viscosity of the models can be measured. The measured viscosities (ν_{I} for model I and ν_{II} for model II) are compared with analytical ν_{a} [calculated by Eq. (46)] in Table I for different e's. Model II agrees well with the analytical

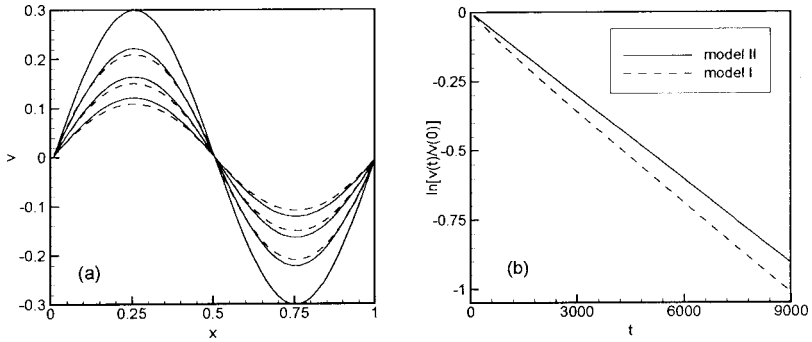

FIG. 2. (a) Distribution of v for $e=0.5$ at $t=0$, 3000, 6000, and 9000 on a lattice: 200×4 (in x and y directions). The dashed lines are for model I and the solid lines are for model II. (b). $\ln[v(t)/v(0)]$ vs t at $x=L/4$.

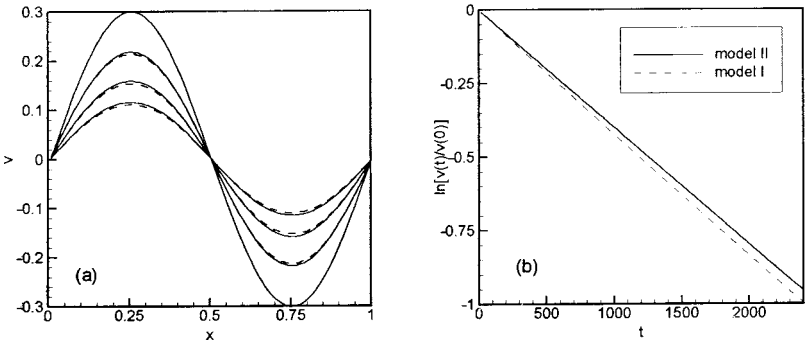

FIG. 3. (a) Distribution of v for $e=2.0$ at $t=0$, 800, 1600, and 2400. The dashed lines are for model I, and the solid lines are for model II. (b) $\ln[v(t)/v(0)]$ vs t at $x=L/4$.

values. Model I has a significant error from the analytical values, and, the smaller e is, the larger the error is. The reason for this is that the viscosity μ decreases with e; therefore, when e is small, the discretion error $\mathbf{B}_1$ becomes more important [see Eq. (44)].

Figure 2(a) shows the profiles of v (for $e=0.5$) at $t=0$, 3000, 6000, and 9000. The dashed lines are for model I and the solid lines are for model II. In Fig. 2(b) the values of $\ln[v(x,t)/v(x,0)]$ are plotted versus t at $x=L/4$ for the two models. They are approximately straight lines. The corresponding viscosity ν is $1.1480[-4]$ for model I and $1.0063[-4]$ for model II. The analytical ν is $9.9691[-5]$.

Figure 3(a) shows the profiles of v (for $e=2.0$) at $t=0$, $t=800$, $t=1600$, and $t=2400$. The dashed lines are for model I and the solid lines are for model II. Figure 3(b) shows the profiles of $\ln[v(x,t)/v(x,0)]$. The difference between the two models are smaller than Fig. 2, because e is larger.

This example demonstrates that model II is more accurate than model I. In the following all the simulations have been carried out by model II.

B. Couette flow

Couette flow provides a good test of the ability of a LB thermal model to describe viscous heat dissipation [17,18]. With the bottom wall fixed and the top boundary moving at the speed of U, the velocity profile is a straight line and the temperature profile satisfies the following relations [17,18] when the variation of the viscosity and heat conductivity can be neglected:

$$T_1 \neq T_0: \quad \frac{T-T_0}{T_1-T_0}=\frac{y}{H}+\frac{\mathrm{Br}}{2}\frac{y}{H}\left(1-\frac{y}{H}\right), \tag{53}$$

$$T_1=T_0: \quad T-T_0=\frac{\mu U^2}{2\kappa}\frac{y}{H}\left(1-\frac{y}{H}\right), \tag{54}$$

where T_0 and T_1 are the temperatures at the bottom and top boundaries, respectively; y is the distance from the bottom boundary; H is the height of the channel; $\mathrm{Br}=\mathrm{Pr}\times\mathrm{Ec}$ is the Brinkman number; $\mathrm{Pr}=\mu c_p/\kappa$ is the Prandtl number; and $\mathrm{Ec}=U^2/c_p(T_1-T_0)$ is the Eckert number. The temperature is defined by $e=c_vT$, and c_v is set to 1.

We used the parameters $\rho_0=1$, $p_0=0.25/1.4$, and $T_0=e_0=p_0/[(\gamma-1)\rho_0]=0.446$, and the corresponding sound speed $c_s=\sqrt{\gamma p/\rho}=0.5$. The domain of computation includes 8×32 nodes (in x and y directions) and is normalized to 1×1. A periodical boundary condition is imposed in the x direction.

Figure 4 shows the results for $T_1=T_0$ (i.e., $\mathrm{Br}=0$), $U=0.25$, 0.5, and 1.5 (i.e., Mach number $\mathrm{Ma}=0.5$, 1, and 3). Figure 4(a) compares the numerical and analytical solutions of the normalized temperature. The solid line in Fig. 4(a) is the analytical solution given by Eq. (54). The numerical results agree well with analytical solutions. Figure 4(b) shows the corresponding velocity profiles for $U=0.25$, 0.5, and 1.5, which are almost straight lines as are the analytical solutions.

Figure 5 shows the results for $T_1=T_0+0.05$ and $U=0.25$, 0.5, 0.707, and 1, i.e., Mach number $\mathrm{Ma}=0.5$, 1, 1.414, and 2, and Brinkman number $\mathrm{Br}=1.25$, 5, 10, and 20. From Fig. 5(a) we can see that the normalized temperature profiles agree well with the analytical solutions (the solid lines) given by Eq. (53). Figure 5(b) shows the corresponding velocity profiles for $U=0.25$, 0.5, 0.707, and 1, which are again almost straight lines. This simulation was also carried out for model I and the similar results were obtained in Ref. [25].

The standard LB model can simulate Couette flow at very low Mach number $0.007\sim0.14$ [17]. In order to increase the Mach number, Chen *et al.* [17] proposed a complex ''higher order model'' and obtained a good solution for Mach numbers up to $M=0.5$. Figures 4 and 5 show that our solutions are in good agreement with the analytical solutions, even when the flow is supersonic.

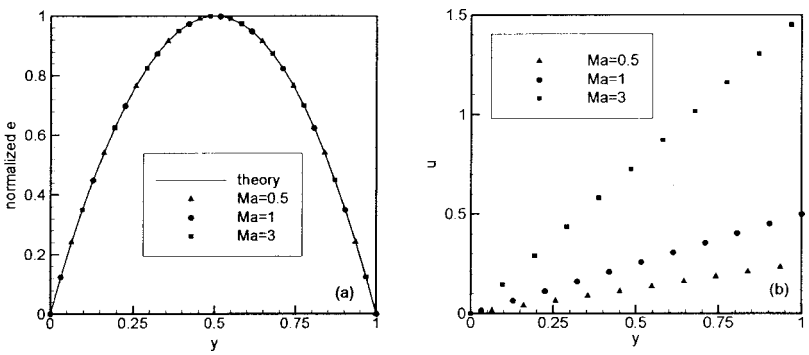

FIG. 4. (a) Energy profiles in Couette flow under different Mach numbers for $T_1=T_0$. The solid line is the analytical solution. (b) Corresponding velocity profiles for $U=0.25$, 0.5, and 1.5.

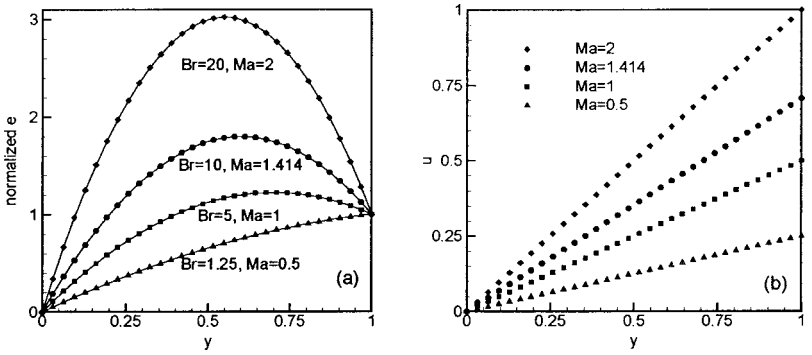

FIG. 5. (a) Energy profiles in Couette flow under different Brinkman numbers for $T_1-T_0=0.05$. The solid lines are the analytical solutions. (b) Corresponding velocity profiles for $U=0.25$, 0.5, 0.707, and 1.

In the last simulation the temperature difference between the two plates is chosen quite small ($dT=T_1-T_0=0.05$) for two purposes: one is to obtain a higher Brinkman number, and the other is to avoid the great variation in the viscosity and heat conductivity that results from the variation in temperature, so that the simulation can be compared with the analytical solutions. Figure 6 shows the velocity profile with $U=0.5$ for different temperature differences $dT=0.05$, 1, and 2. The deviations from the linear profile are visible for $dT=1$ and 2, due to the great variation in temperature.

C. Shock reflection on an invisid wall

If we regard the viscous terms and the diffusion terms of the right-hand sides of Eqs. (44) and (45) as the discretion error, Eqs. (43), (44), and (45) become an inviscid Euler system. In fact, the viscosity and diffusivity are of order $(\tau-\frac{1}{2})l^2/\Delta t$, where l is the unit length of the lattice and Δt is the unit time. We have performed a 29° shock reflection for $\tau=1$ and $\gamma=1.4$.

The computational domain is a rectangle of length 3 and height 1 divided into 360×140 nodes. Dirichlet conditions are imposed on the left and upper boundaries, respectively:

$$(\rho,u,v,p)|_{(0,y,t)}=(1.0,\ 0.5\times2.9,\ 0.0,\ 0.25/1.4),$$

$$(\rho,u,v,p)|_{(x,1,t)}=(1.69997,\ 0.5\times2.61934,\ -0.5\times0.50633,\ 0.25\times1.52819).$$

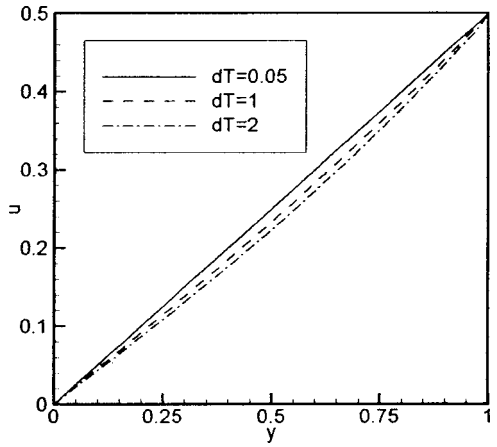

FIG. 6. Velocity profiles in Couette flow with $U=0.5$ for different temperature differences, $dT=0.05$, 1, and 2.

The bottom boundary is a reflecting wall (see Fig. 7), corresponding to slip condition. Initially, the solution of the entire domain is set to be that at the left boundary [19]. The corresponding Mach number is 2.9. Figures 8(a) and 8(b) show the pressure and density contours. The clear shock reflection on the wall agrees well with the exact solution. It is noted that the shocks are much finer than those of our previous results [2] (280×80 grids) and than those of the kinetic flux vector splitting methods (80×20 [20] and 60×20 [21] grids) because the pressure is smaller (therefore μ and κ are smaller) and the lattice is finer (360×140). The main purpose of this simulation is to compare the shock reflection on a slip wall with that on a nonslip wall presented in the next simulation.

D. Interaction between shock and boundary layer

In this example, a nonslip condition on the bottom wall was set. All the other conditions are the same as those in Sec. III C, including the lattice condition, initial conditions, and boundary conditions on entrance, exit, and upper wall. On the bottom wall, the following conditions were imposed: a nonslip wall, $u=0$, $v=0$; a zero pressure gradient in y direction, $\partial p/\partial y=0$; and a constant temperature $e=$const. The density was then determined by the state equation for perfect gas.

Figures 9(a), 9(b), 9(c), and 9(d) display the pressure, density contour, u contour, and streamlines. Figures 9(c) and 9(d) clearly show the boundary layer structure. Because of the great adverse pressure gradient crossing the shock, the boundary layer separation occurs at about $x=1.6$, where the shock reaches the boundary layer; thereafter the boundary layer reattaches, corresponding to the curved streamlines which are convex in the direction of the wall. From Fig. 9(a) we can see that the leading edge of the bottom wall disturbs the uniform inlet flow, and induces a shock which turns slightly to the right after traversing the oblique shock. The impinging oblique shock is similar to that in Sec. III C before it reaches the boundary layer. However, the reflected pattern contains a system of compression and expansion waves, after which another fan of compression waves is formed. The boundary thickness increases ahead of the point of arrival of the oblique shock. The boundary layer exhibits a large local

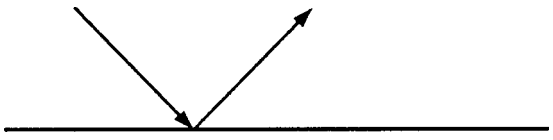

FIG. 7. Particle reflection on a slip wall.

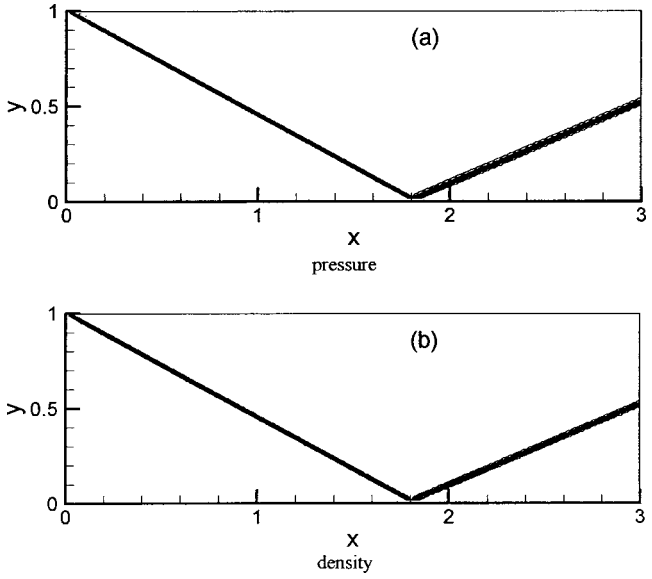

FIG. 8. Shock reflection on a slip wall. Grid size: 360×140. Pressure (a) and density (b) contours at $t=1000$.

thickening which leads to a separation. This situation agrees with that described in Ref. [22].

IV. CONCLUSION

We have proposed an improved adaptive thermal LB model for viscous compressible flows. The proper heat conduction term in the energy equation is restored, and the discretion error is eliminated. This model can handle flows over a wide range of Mach numbers and capture shock jumps. The adaptive nature of the particle velocities makes a link between the LB model and the discrete-velocity models [23]. The BGK Boltzmann equation is the basic equation. The Navier-Stokes equations were derived by the Chapman-Enskog method. One-dimensional simulations for sinusoidal velocity distributions were performed in order to check the viscosity. The velocity distributions were compared with the analytical solution, and the measured viscosities were compared with the theoretical values. Because of the absence of a discretion error, model II agrees better with the analytical solution than model I. The numerical results for the Couette flow agrees well with analytical solutions even when the flow is supersonic. In the simulation for the reflection of an oblique shock impinging on a solid wall, the complex structure of the shock wave, resulting from the interaction between the shock and the boundary layer, was well captured. The total computation time is proportional to the total number of nodes. This model retains most of the advantages of the standard lattice Boltzmann method, such as parallelism of the method, and ease of programming. Another advantage of this model is that the boundary condition imposed for the macroscopic variables can be easily realized because the calculation at each iteration starts by the macroscopic variables, independent of the details of particle distributions. The

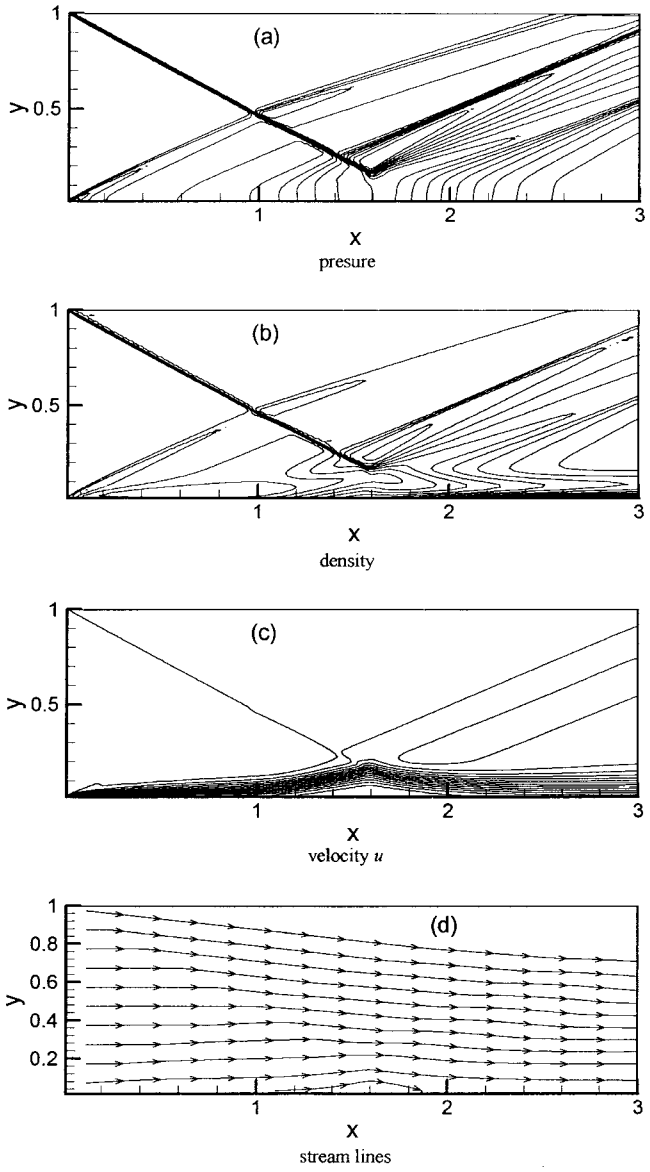

FIG. 9. Interaction between shock and boundary layer on nonslip wall. (a) Pressure, (b) density, (c) u contours, and (d) streamlines at $t=1000$. Grid size: 360×140.

model is as efficient as the standard LB models and consumes less computer memory, because we have taken advantage of the condition $\tau=1$ in the numerical simulations; otherwise, the simulations would require enormous computer memory and time.

ACKNOWLEDGMENTS

The author thanks D. Bernardin, O. Sero-Guillaume, S. Chen, H. Chen, D. Doolen, and S. Succi for helpful discussions. This work was supported by the National Natural Science Foundation of China (Grant Nos. 19672030 and 19972037) and by the Scientific Research Foundation for Returned Overseas Chinese Scholars, State Education Ministry.

[1] S. Chen and G.D. Doolen, Annu. Rev. Fluid Mech. **30**, 329 (1998).
[2] C.H. Sun, Phys. Rev. E **58**, 7283 (1998).
[3] G. Yan, Y. Chen, and S. Hu, Phys. Rev. E **59**, 454 (1999).
[4] U. Frisch, B. Hasslacher, and Y. Pomeau, Phys. Rev. Lett. **56**, 1505 (1986).
[5] U. Frisch, D. d'Humières, B. Hasslacher, P. Lallemand, Y. Pomeau, and J.P. Rivet, Complex Syst. **1**, 649 (1987).
[6] H. Chen, S. Chen, and W. Matthaeus, Phys. Rev. A **45**, R5339 (1992).
[7] Y.H. Qian, D. d'Humières, and P. Lallemand, Europhys. Lett. **17**, 479 (1992).
[8] R. Benzi, S. Succi, and M. Vergassola, Phys. Rep. **222**, 145 (1992).
[9] K. Xu, J. Stat. Phys. **81**, 147 (1995).
[10] K. Xu, L. Martinelli, and A. Jameson, J. Comput. Phys. **120**, 48 (1995).
[11] B.T. Nadiga, J. Stat. Phys. **81**, 129 (1995).
[12] F.J. Alexander, H. Chen, and G.D. Doolen, Phys. Rev. A **46**, 1967 (1992).
[13] Y.H. Qian and S.A. Orszag, Europhys. Lett. **21**, 255 (1993).
[14] S.X. Hu, G.W. Yan, and W.P. Shi, Acta Mech. Sin. **13**, 314 (1997).
[15] D. Bernardin, O. Sero-Guillaume, and C.H. Sun, Physica D **47**, 169 (1991).
[16] C. H. Sun, Ph.D. thesis LEMTA, L'Institut National Polytechnique de Lorrain, Nancy, France, 1993 (unpublished).
[17] Y. Chen, H. Ohashi, and M. Akiyama, J. Stat. Phys. **81**, 71 (1995).
[18] X. He, S. Chen, and G.D. Doolen, J. Comput. Phys. **146**, 282 (1998).
[19] P. Colella, J. Comput. Phys. **87**, 171 (1990).
[20] J.C. Mandal and S.M. Deshpande, Comput. Fluids **23**, 447 (1994).
[21] K. Xu and K.H. Prendergast, J. Comput. Phys. **114**, 9 (1994).
[22] D. Schlichting, *Boundary Layer Theory*, 6th ed. (McGraw-Hill, New York, 1968).
[23] R. Gatignol, *Lecture Notes in Physics* (Springer-Verlag, Berlin, 1975), Vol. 36.
[24] G.A. Sod, J. Comput. Phys. **27**, 1 (1978).
[25] C.H. Sun, Chin. Phys. Lett. **17**, 209 (2000).